



# Anatomy of the Tsunami and Lamb Waves-Induced Ionospheric Signatures Generated by the 2022 Hunga Tonga Volcanic Eruption

EDHAH MUNAIBARI,<sup>1</sup>  LUCIE ROLLAND,<sup>1</sup> ANTHONY SLADEN,<sup>1</sup> and BERTRAND DELOUIS<sup>1</sup>

**Abstract**—As tsunamis propagate across open oceans, they remain largely unseen due to the lack of adequate sensors. To address this fundamental limitation of existing tsunami warnings, we investigate Global Navigation Satellite Systems (GNSS) data to monitor the ionosphere Total Electron Content (TEC) for Traveling Ionospheric Disturbances (TIDs) created by tsunami-induced internal gravity waves (IGWs). The approach has been applied to regular tsunamis generated by earthquakes, while the case of undersea volcanic eruptions injecting energy into both the ocean and the atmosphere remains mostly unexplored. With both a regular tsunami and air-sea waves, the large 2022 Hunga Tonga-Hunga Ha’apai volcanic eruption is a challenge. Here, we show that even in near-field regions (1000–1500 km), despite the complex wavefield, we can isolate the regular tsunami signature. We also highlight that the eruption-generated Lamb wave induces an ionospheric disturbance with a similar waveform and an amplitude spatial pattern consistent with IGW origin but with a quasi-constant propagation speed ( $\sim 315$  m/s). These results imply that when GNSS-TEC measurements are registered near an ocean bottom pressure sensor, they can help discriminating the regular tsunami from the initial air-sea waves appearing in the sensor observations.

**Keywords:** Ionosphere monitoring, tsunami detection, global navigation satellite systems (GNSS), traveling ionospheric disturbances (TIDs), tsunami warning systems, internal gravity waves (IGWs).

## 1. Introduction

Tsunamis are natural hazards that have already claimed the lives of more than 250,000 civilians globally (Mizutori & Guha-Sapir, 2018). Tsunamis are commonly monitored on shores by coastal tide

gauges or in deep oceans by tsunami buoys. These instruments provide direct measurements of the tsunami but can be insufficient for early warnings because (1) tide gauges are located on the coasts, giving little to no time for a warning, and (2) tsunami buoys are expensive to deploy and maintain, resulting in a limited sampling of the oceans, not sufficient for near-field warning. An alternative but indirect method centers around the computation of the ionospheric total electron content (TEC) to track tsunami propagation. TEC is a parameter commonly used to study and investigate the state of the ionosphere (Ratcliffe, 1951), which is the layer containing the ionized part of Earth’s upper atmosphere and stretches from approximately 50 km to more than 1000 km. The established definition of the total electron content is the total number of electrons integrated between two points along a column of a meter-squared cross-section according to the following expression

$$TEC = \int n_e(s) ds, \quad (1)$$

where  $ds$  is the integration path and  $n_e(s)$  is the location-dependent electron density (Evans, 1957). There are different methods developed to obtain ionospheric TEC measurements from observations such as the Faraday Rotation effect on a linear polarized propagating plane wave (Titheridge, 1972). However, today TEC measurements are made mostly using GNSS (Global Navigation Satellite Systems) data. By utilizing the delay imposed by the ionosphere on the signal sent by a satellite, TEC values can be computed. For example, in the case of satellites equipped with dual-frequency systems, the ionospheric delay in meters is found according to

---

**Supplementary Information** The online version contains supplementary material available at <https://doi.org/10.1007/s00024-023-03271-5>.

---

<sup>1</sup> Université Côte d’Azur, Observatoire de la Côte d’Azur, CNRS, IRD, Géoazur, 250 rue Albert Einstein, Sophia Antipolis, 06560 Valbonne, France. E-mail: edhah.munaibari@geoazur.unice.fr

$$I = \frac{40.3(f_1^2 - f_2^2)}{f_1 f_2} 10^{16} \text{TEC}, \quad (1)$$

where  $I$  can be computed by taking the difference of the two measurements of pseudo-range or that of carrier phase obtained by a GNSS receiver station and  $f_1$  &  $f_2$  are the two frequencies used by the satellites to transmit signals back to the ground stations (Liu et al., 1996). The first tsunami-induced ionospheric (TEC) signature was presented by Artru et al. (2005) following the tsunami generated by the Jun. 23 2001 8.4 Mw Peruvian earthquake, and since, this technique has been used to identify and characterize the TEC signatures of a variety of tsunamis, all initiated by submarine earthquakes (Galvan et al., 2011; Grawe & Makela, 2015, 2017; Liu et al., 2006; Rolland et al., 2010). Underwater volcanic eruptions and landslides can also trigger tsunamis, except that there haven't been many large instances in the last decades to study them in the light of modern instrumentation. The 2022 explosion of the Hunga Tonga-Hunga Ha'apai (HTHH) submarine volcano provides a unique opportunity to fill this gap and characterize the generated ionospheric perturbations.

According to the US Geological Survey (USGS), the HTHH volcano (20.546°S 175.39°W; Fig. 1a) violently erupted on Jan. 15, 2022, at 4:14:45 UTC (17:14:45 LT). The eruption released a massive ash plume that reached an altitude of ~55 km (Smart, 2022). It also generated a highly-energetic atmospheric Lamb wave observed globally (for a few days after the eruption) in different types of measurements (e.g., barometers, infrasound sensors, satellites images, ionospheric measurements) (Amores et al., 2022; Matoza et al., 2022; Wright et al., 2022; Zhang et al., 2022). According to Themens et al. (2022), large and medium-scale traveling ionospheric disturbances (TIDs) appeared in global TEC measurements following the eruption, with travel speeds ranging from 200 to 1000 m/s. They attributed the two TIDs types to the initial acoustic response of the explosive eruption and the energetic Lamb wave, respectively. The same findings were reported by Lin et al. (2022), where they also reported the presence of conjugate TIDs. In addition, Astafyeva et al. (2022) used the nearfield TEC measurements to identify the presence of several volcanic explosions during the event

timeline. Moreover, the Lamb-wave overpressure coupled with the ocean triggering fast traveling air-sea (pressure-forced tsunami-like) waves observed worldwide (Kubota et al., 2022; Lynett et al., 2022; Omira et al., 2022). According to Matoza et al. (2022), the Lamb wave signature appears to be consistent (arrival time, waveform) in both the ionospheric and sea-level observations. Furthermore, Kulichkov et al. (2022) reported the presence (in certain regions; Puerto Rico and Catania) of two oppositely-propagating air-sea waves. The first was generated by the Lamb wave traveling away from the volcano toward its antipode and the second by the Lamb wave traveling from the antipode toward the volcano.

The eruption also produced a classical tsunami, i.e., from direct water mass displacement, detected across the Pacific Ocean (Carvajal et al., 2022), causing four casualties in Tonga (Latu, 2022) and two in Peru (Parra, 2022). The exact mechanism triggering the tsunami is not well-understood yet, but preliminary analysis suggests a combination of submarine explosion and caldera collapse (Hu et al., 2023 and reference therein). An ionospheric signature of this tsunami was reported by Matoza et al. (2022) at near-field. Here, we strengthen the study with a spatial pattern analysis and expand the investigated dataset more globally (Pacific-wide). We seek to isolate the ionospheric signature of the tsunami from the acoustic and Lamb signals. Because of these multiple, partially overlapping signals, we do not expect the discrimination to be straightforward, yet, it is a necessary step to assess the potential of TEC data for tsunami early-warning even in the case of a volcanic eruption.

To support our TEC signal analysis, we first analyze the case of the tsunami produced by the Mw 8.1 Kermadec earthquake, which occurred a year before, on March 4th, 2021 about 1000 km South of Tonga (29.723°S 177.279°W, based on the USGS report) (Fig. 1a). Both events occurred in the western region of Polynesian islands sparsely equipped with GNSS stations installed onland. The size of the tsunami triggered by the Kermadec earthquake was smaller than the one triggered by the HTHH event by less than one order of magnitude (respectively 3 and 20 cm in the near-field after Romano et al., 2021 and

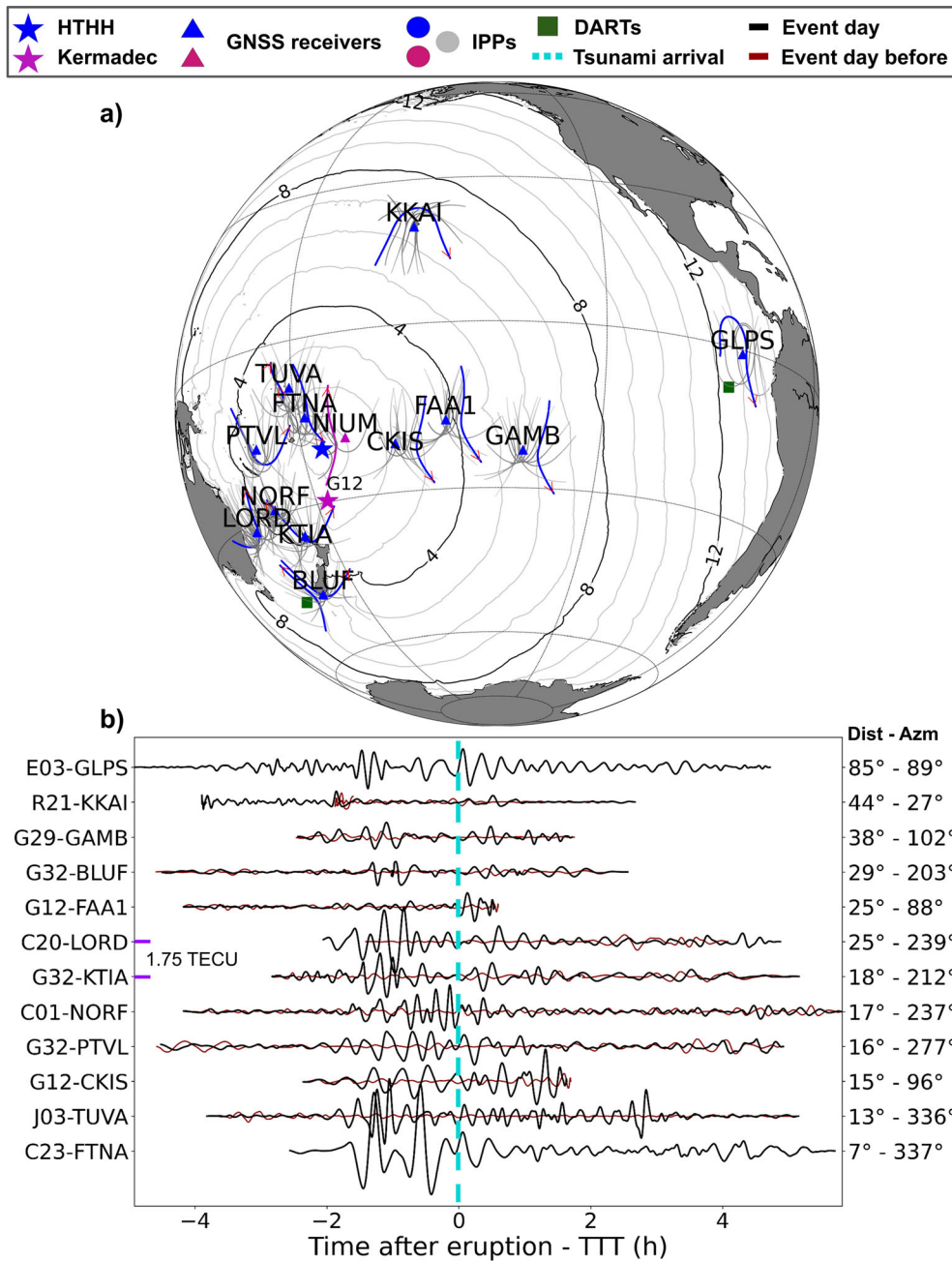


Figure 1

**a** Context map of the study with locations of the tsunami sources and measurements. The Jan. 15, 2022, Hunga Tonga-Hunga Ha’apai volcanic eruption and the Mar. 4, 2021, 8.1 Mw Kermadec Islands earthquake epicenter are marked with a blue and purple star, respectively. GNSS receivers are marked with triangles of the same color. The contours highlight the Hunga theoretical tsunami traveling times (TTT) in hours. Ionospheric Pierce Points (IPPs at 300 km altitude) are depicted by colored dots for the selected pairs, while gray dots represent that of other pairs. **b** A selection of filtered sTEC measurements with tsunami-induced signature. Satellites are marked with a letter: Beidou (C), QZSS (J), GPS (G), GLONASS (R), Galileo (E), and PRN number. To highlight the tsunami signature, the time series are aligned with respect to the tsunami theoretical arrival time (TTT)

Lynett et al., 2022). We thus use the Kermadec event as a test case to help decipher the HTHH tsunami-induced ionospheric signature with a sparse multi-GNSS network.

In addition to presenting the ionospheric signatures of the two tsunamis, we investigate how the tsunami generation mechanism (earthquake vs. volcano) affects their detection. We compare the tsunami sea-level variations to the identified ionosphere disturbances to confirm the tsunami origin of the detected ionospheric imprints. Finally, we examine the ionospheric response of the Lamb wave the HTHH eruption produced and compare it to that of the tsunami. Our goal is to discriminate the tsunami-induced ionospheric signature from the Lamb wave signature. The correct identification of the former is indeed critical for constraining the tsunami wave height in the ocean (Rakoto et al., 2018) and avoiding false alarms.

## 2. Data and Methods

The previous detections of tsunami-induced TEC-based ionospheric signatures in the literature are based on the use of dense networks of GNSS receivers (Grawe & Makela, 2017 and references therein). Here, the sparsity of GNSS receivers in the south Pacific area requires a single receiver approach to identify the tsunami's ionospheric response and study its evolution at various distances and directions. To test the single receiver technique, we examine the Kermadec tsunami through the GNSS receiver located in Niue Island (NIUM; Fig. 1a), ~1400 km from the epicenter. Such distance favors the detection of both the earthquake and the tsunami ionospheric signatures (Fig. 1a). While the coseismic acoustic gravity wave (AGW) can be observed next to the source, the IGW triggered by the tsunami cannot be observed closer than 500 km from the source and sooner than 40 min to 1 h after the initiation because the atmospheric wave also needs to propagate vertically (Fig. 2) at a speed below 100 m/s (Occhipinti et al., 2013). For tsunami early-warning, these properties make the AGW measurements more suited in the near-field (Zedek et al., 2021) and the tsunami-induced IGW measurements more suited in the

medium and far-field (this study). Very few studies are focusing on tsunami-induced IGWs. Indeed, they are more rare and more challenging to pinpoint as AGWs display higher amplitudes and also accompany non-tsunamigenic earthquakes (Heki et al., 2022; Zedek et al., 2021).

From the NIUM GNSS observation data, we compute the raw slant total electron content (sTEC) and apply a sequence of filters (polynomial detrend, apodization, and band-pass filter; see Text S1 in the Supplementary Material SM for a detailed description). The bottom panel of Fig. 3a depicts the raw sTEC (to check the absence of artifacts; e.g. caused by cycle slips) observed by the satellite-receiver pair G12-NIUM. The top x-axis in the panel indicates the satellite elevation where we applied a mask removing data below 20° elevation (unlike the 10° mask adopted for the rest of this work) to minimize the possible artifacts enhanced by the low elevation (see G12 in Fig. 4a). After that, we use the theoretical tsunami travel times (TTT) to estimate the expected tsunami arrival time at a particular location (e.g., sTEC data IPPs location [see Fig. 2]: the intersection of the line of sight with the ionosphere shell at a certain altitude [Davies & Hartmann, 1997], 300 km in this study), knowing that the associated TEC signature should appear approximately around the same time (Rolland et al., 2010). These processing steps allow us to observe two distinct signatures: the earthquake acoustic response (A) appearing ~10 min after the initiation time (IT) (Liu et al., 2010 and references therein) and the tsunami emerging within the expected arrival time (T). This pattern is consistent over the different satellites seen by the receiver (Fig. 4a). The spatial pattern of the maximum TEC amplitude around the receiver further assesses the detection. According to Georges and Hooke (1970), the TEC amplitude of tsunami-induced IGWs increases from upstream (line-of-sight LOS crosses the IGW phase fronts; lower maximum TEC amplitude) to downstream (LOS lying along the IGW phase fronts; larger maximum TEC amplitude) of the receiver as a result of the alignment between the LOS and the IGWs phase front (Fig. 2; Fig. 4c). Within this work, we refer to this phenomenon as the IGWs pattern of the detected signatures' maximum TEC amplitude. The technique's applicability is

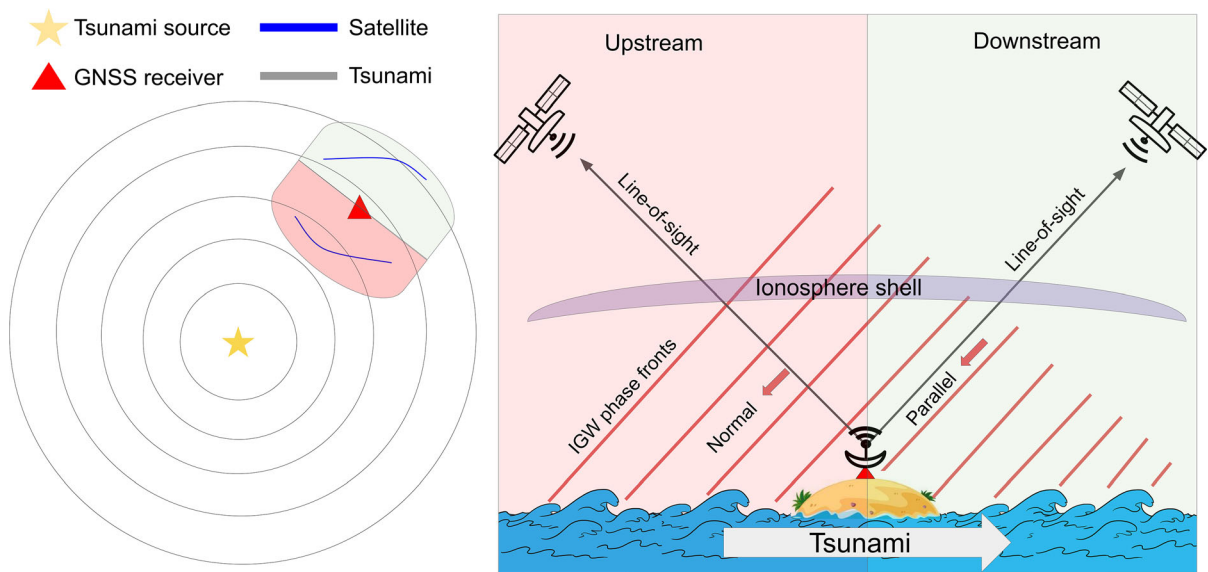


Figure 2

Schematic illustration of the receiver upstream/downstream concept (Adapted from Grawe & Makela, 2015) where the alignment between the line-of-sight (LOS) and the tsunami-induced IGW phase fronts play a significant role in the amplitude of the detected ionospheric TEC disturbances since TEC is an integrated LOS measurement. LOSs normal to the IGW phase fronts incline to generate lower amplitudes, while those parallel to the phase fronts incline to generate larger amplitudes

made possible thanks to multi-GNSS observations with an efficient azimuthal coverage that increases the reliability of the detection.

We follow the same procedure for the HTHH tsunami, selecting GNSS receivers located in several Pacific islands (Fig. 1a; Table S2 in SM), to extend our analysis with more global coverage. The detection made by each receiver is independent of the others. We selected receivers with multi-GNSS capability. The chosen receivers fall in a distance ranging from 700 to 10 000 km, and thus from near to far field, with respect to the tsunami source. This allows us to track the fully-developed tsunami in the ionosphere as it travels across the Pacific.

### 3. Results

#### 3.1. Tsunami-Induced TEC Signatures Across the Pacific Ocean

We identified the ionospheric signatures of the HTHH tsunami in the TEC data from 12 receivers around the Pacific (Fig. 1b). The tsunami-induced ionospheric signatures are corroborated by

observations from other satellites for each receiver (Fig. 4 to 13 in SM). The tsunami TEC amplitude and the local tsunami arrival time of the twelve series are illustrated in Table S2 of the SM. These results agree with the dense-network-based study of Ravanelli et al., accepted for publication in GRL, 2023 (specifically in the vicinity of New Caledonia and New Zealand).

Applying our detection method with the GNSS receiver located on Lord Howe Island (LORD; Fig. 1a) during the generation and passage of the HTHH tsunami, we successfully identified its ionospheric signatures, as confirmed by the two-step verification procedure (Fig. 4b, d). By comparing the Kermadec and HTHH signatures (Fig. 3a, b), we see how exceptional the HTHH event is; a complex time series with multiple types of waves, and an amplitude one order of magnitude larger (Table S2 in SM).

#### 3.2. Ionospheric Signatures Comparison (Earthquake-Induced vs. Volcanic Eruption-Induced)

To investigate the impact of the trigger source (earthquake vs. volcanic eruption) on the induced

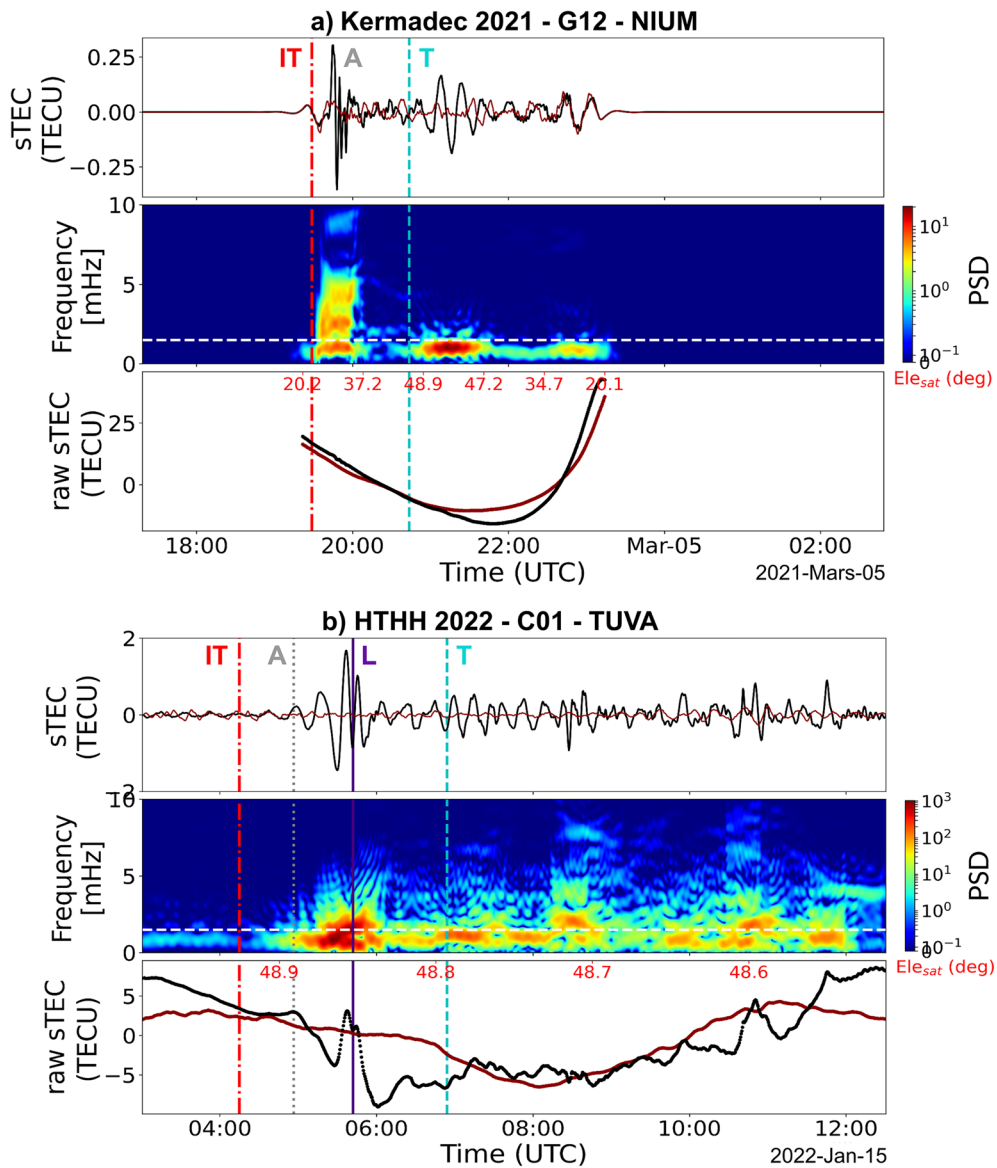


Figure 3

Comparison between the ionospheric TEC waveforms obtained by the satellite-receiver pairs G12-NIUM (Kermadec) and C01-TUVA (HTHH). **a** TEC measurements during the Kermadec earthquake and the passage of the triggered tsunami. The three panels from bottom to top are: the raw-unfiltered sTEC, the event day filtered sTEC spectrogram, and the filtered sTEC. The filtered sTEC is zero-padded to match the length of C01-TUVA. The vertical red line represents the event initiation time (IT). The top x-axis shows the satellite's elevation. The horizontal white line in the spectrogram indicates the expected frequency of tsunami ionospheric signature (i.e., 1.5 mHz; 11 min). **b** TEC measurements during the HTHH volcanic eruption and the produced tsunami passage. The expected arrival times of the acoustic pulse A; 667 m/s, the Lamb wave L; 318 m/s (Wright et al., 2022) and the tsunami are highlighted

ionospheric signatures of a tsunami, we focus on two TEC measurements with optimal configuration (the orientation of the tsunami aligns with the local geomagnetic field, and the favorable observing

geometry; the angle between the line-of-sight and the IGWs phase front favors observation of large TEC variation; Georges & Hooke, 1970): G12-NIUM (Kermadec; Fig. 3a) and C01-TUVA (HTHH;

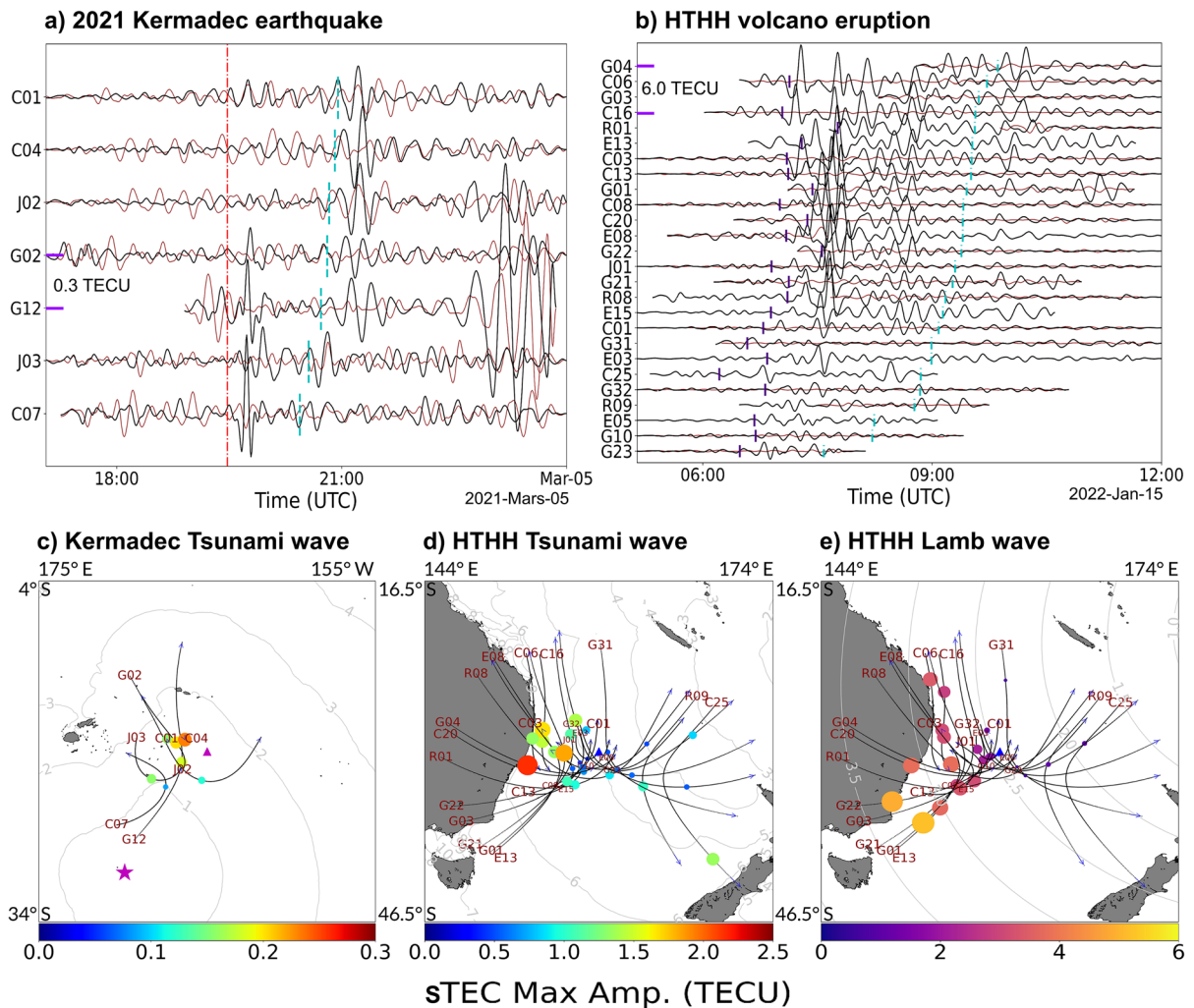


Figure 4

**a** The tsunami-induced ionospheric signatures detected in the vicinity of Niue Island (NIUM) after the 2021 Kermadec earthquake. **b** The ionospheric signatures detected in the vicinity of Lord Howe Island (LORD) induced after the HTHH volcanic eruption. **c** Geographic view of the earthquake's epicenter, the GNSS receiver, and the ionospheric tracks of the satellites whose sTEC time series are shown in **a**. Along the satellites' tracks, the disks indicate the satellites' locations at the tsunami expected arrival time, whose size and color point out the detected maximum sTEC amplitude of the selected waveform. The max sTEC amplitude is calculated within a 2 h observation window starting 15 min before TAT as  $\frac{\max_{obs} - \min_{obs}}{2}$ . **d** Map showing the GNSS receiver and the ionospheric tracks of the satellites whose sTEC time series are shown in **b**. **e** The disks depicted in the map show the satellites' locations at the Lamb wave arrival, with their size and color representing the wave's maximum sTEC amplitude. The results illustrated by **c**, **d**, and **e** demonstrate that the filtered sTEC amplitude downstream of the receiver is larger than upstream, as expected from IGWs

Fig. 3b). Both are located in the medium field ( $\sim 1400$  km) and are band-pass filtered from 0.7 to 10 mHz.

For the Kermadec event, we observe two remarkable signatures that we link to the event. The first signature is the earthquake acoustic response appearing  $\sim 10$  min after the initiation as an N-shape pulse,

as routinely observed after earthquakes (Liu et al., 2010 and references therein). We have consistent arguments supporting that the second signature is that of the tsunami: (1) it occurs within the expected arrival time of the tsunami, (2) it has an oscillatory signature with a clear frequency peak at 1.2 mHz, in the range of what is expected for the tsunami waves,

(3) it is supported by the different satellites seen by the receiver (Fig. 4a), and (4) the IGWs pattern of the detected signatures' maximum TEC amplitude (Fig. 4c).

Unlike the Kermadec submarine earthquake, the HTHH submarine volcanic eruption ionospheric waveforms are more complex and present a richer spectrum (Fig. 3b). Beside the signature of the initial acoustic response (arrival time A), a Lamb wave (arrival time L) is visible in the volcano eruption data as a double pulse of maximum amplitude 1.56 TECU. The response of the tsunami then emerges at the expected arrival time (T) with an amplitude of 0.58 TECU. In contrast to the earthquake case, the ionosphere during the eruption experiences higher disturbances related to the main, massive, explosion of the eruption, and the numerous different types of waves it injected into the Earth's atmosphere (Wright et al., 2022). In addition, the eruption took place during the early recovery phase of a moderate geomagnetic storm (Lin et al., 2022), which is known to largely disturb the ionospheric background (higher noise in GNSS TEC signals; Fagundes et al., 2016). Such disturbances can also be seen in some of the sTEC series shown in Fig. 1 (see also Fig. 4b), especially those close to the volcano.

### 3.3. Ionosphere vs. Pressure Measurements

To further assess the tsunami origin of the identified imprints, we compared the sTEC disturbance measured offshore Galapagos Islands with the sea-level anomaly registered by a deep-sea ocean-bottom pressure DART buoy #32413 about 800 km southwest of the islands (Fig. 1a). Both signals have similar waveforms with a peak frequency around 1.2 mHz (Fig. 5a). The emergence of the signal 30 min earlier in the ionosphere suggests two scenarios (or a combination of the two); (1) either the shoaling of the bathymetry around the Galapagos archipelago slowed down the tsunami in the sea surface while allowing its induced IGWs to advance ahead of it, (2) or as IGWs are dispersive packets of waves (Vadas et al., 2015), waves with shorter intrinsic frequency and longer horizontal wavelengths propagate ahead of the tsunami, while waves with higher intrinsic frequency and short horizontal

wavelengths propagate behind the tsunami (Inchin et al., 2020). A similar effect was observed for the 2011 Tohoku tsunami when it approached Hawaii (Occhipinti et al., 2011).

We also note the presence of an ionospheric signature having an amplitude and a spectral content similar to the tsunami waveform but 2 h earlier (Fig. 5a). It appears to travel with a speed of  $\sim 233$  m/s and could be linked to an IGW triggered by the eruption and traveling all the way in the atmosphere.

### 3.4. Ionospheric Signatures of the Lamb Wave

When examining the ionospheric (TEC) data as we search for the HTHH tsunami signatures, we first notice the peculiar waveform of the Lamb wave, whose raw sTEC measurements display massive decreases and increases that resemble a large W-shape (Fig. 15 in SM). The Lamb wave processed imprints exhibit close similarity to the Tsunami's. We note that the ionospheric signature of both the Lamb and the tsunami waves peak at a similar frequency of 1.2 mHz (Fig. 3b), with the Lamb wave displaying a more impulsive behavior. Furthermore, Fig. 4e shows that the Lamb wave's imprint' maximum sTEC amplitude spatial pattern exhibits an IGW pattern (similar to the tsunamis cases in Fig. 4c and 4d), where the maximum amplitude is larger downstream of the GNSS receiver. Overall, the Lamb wave signature has a larger amplitude than the tsunami signature.

We also investigated the co-located measurements of a Lamb wave (plus the air-sea waves) signature measured at sea level by the ocean-bottom pressure buoy DART #55015 and its ionospheric signature in southern New Zealand (Fig. 5b). They both show an impulsive N-shape waveform (in the time domain) and a broadband frequency content (Fig. 5b). These observations are consistent with pressure simulation results (Amores et al., 2022; Gusman et al., 2022) and ionospheric signatures retrieved over New Zealand (Ajith et al., 2022; Zhang et al., 2022). In addition, when corrected for the travel time (see Fig. 16 in SM), assuming a range of 310–320 m/s horizontal propagation speed, the signatures show a 5 to 1 s delay between the arrival at



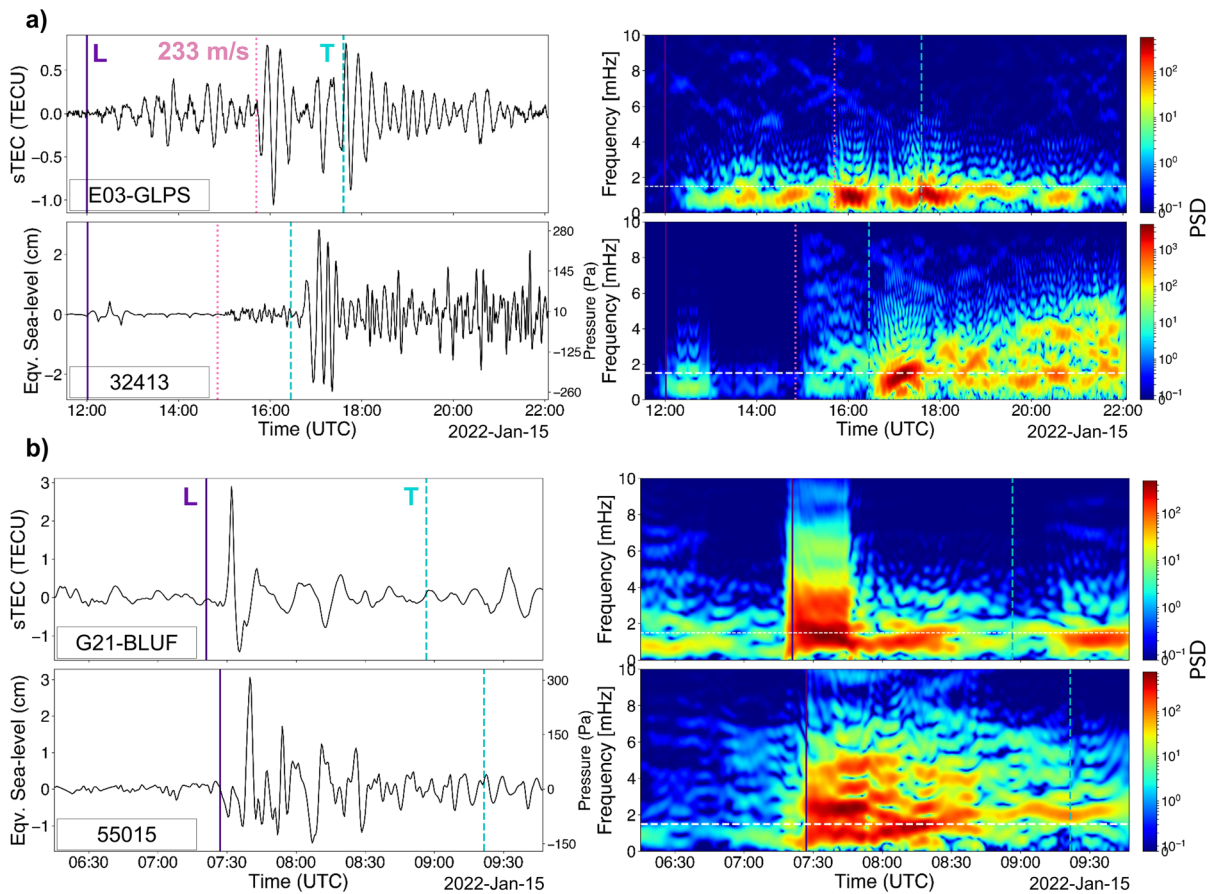


Figure 5

Comparison between ocean bottom pressure-based surface anomaly and ionospheric signatures in the vicinity of Galapagos Islands (a) and southern New Zealand (b) on Jan. 15, 2022. Time series are on the left, and spectrograms are on the right. (a) The top panel shows the filtered E03-GLPS sTEC measurements. The bottom panel presents the pressure (sea-level equivalent) measurements from the tsunami buoy DART 32413. (b) The top panel is the sTEC measurements of G21-BLUF, and the bottom is the pressure (sea-level equivalent) observation of DART 55015. The results show that the Lamb wave is better sensed in the vicinity of southern New Zealand, whereas near the Galapagos Islands, the tsunami is

the Buoy's location and the ionosphere, assuming a 300 km IPP height, with the pressure signature appearing first. The amplitude pattern (see Fig. 17 in SM), and small time delay suggest that in the same way as the tsunami, the Lamb wave triggered internal gravity waves (IGWs), which traveled upward to ionospheric heights with the approximately same horizontal speed as the Lamb wave.

#### 4. Discussion

The global overview of the ionospheric imprint amplitude shows interesting features (Fig. 1). The

tsunami's smallest sTEC amplitude is observed in Hawaii. Three possible reasons could have caused the lower amplitude aside from the tsunami open-ocean size itself ( $\sim 6$  cm zero to crest recorded by the 51407 DART buoy): (1) the local time of the tsunami arrival was around 1 am (Table S2), meaning a low ionization rate (compared to the daytime) and consequently a smaller amplitude of detected signatures (Grawe & Makela, 2015), (2) the inefficient coupling between the tsunami-induced IGWs and the local geomagnetic field (Occhipinti et al., 2008), or (3) the destructive interaction between the conjugate Traveling Ionospheric Disturbances (TIDs) and the direct TIDs traveling away from the volcano as suggested

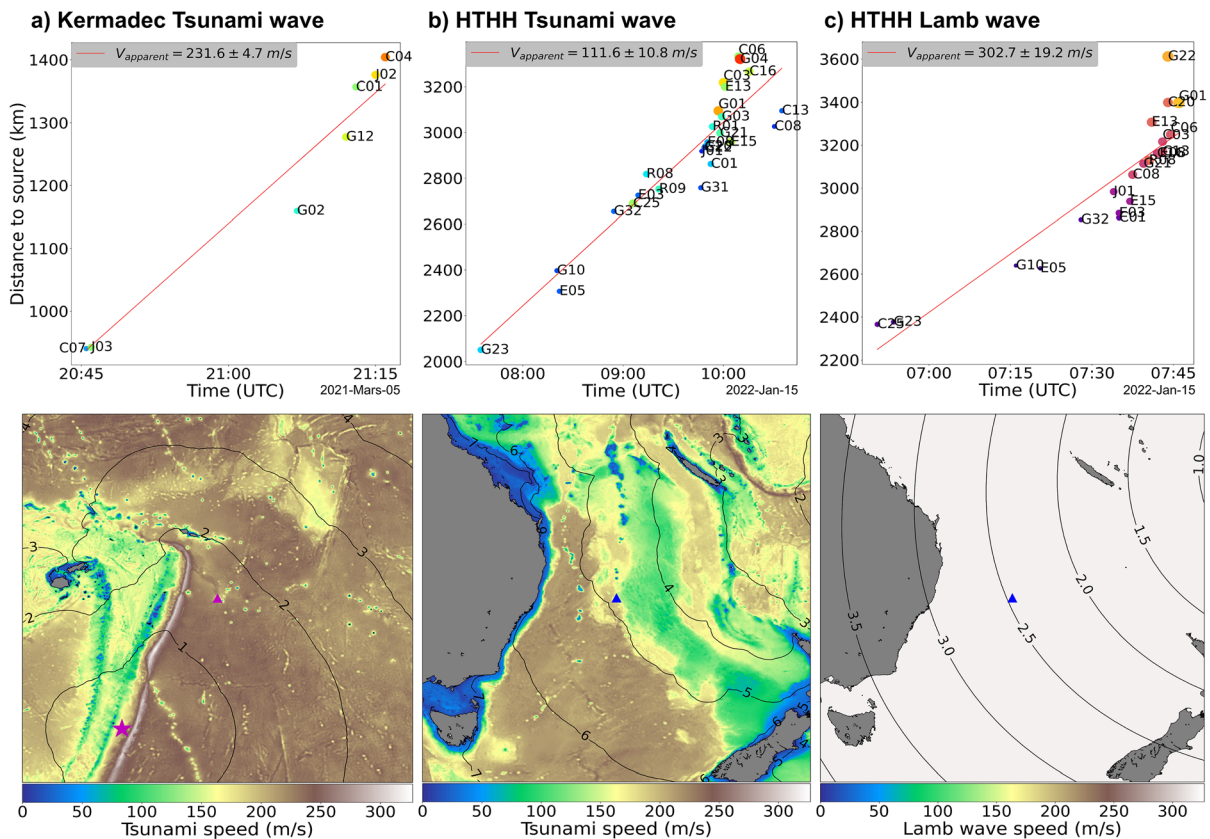


Figure 6

Travel-time distance plot of the TID signature maximum energy (colored disks), and linear fit (red line) with propagation speed estimation (top) compared to the theoretical propagation speed (bottom). **a** tsunami signature in the vicinity of Niue Island (NIUM) after the 2021 Kermadec earthquake **b** tsunami signature in the vicinity of Lord Howe Island (LORD) induced after the HTHH volcanic eruption and **c** Lamb wave signature in the vicinity of Lord Howe Island (LORD) after the HTHH volcanic eruption. The three maps display the same geographical view as Fig. 4c, d, and e respectively

by Themens et al. (2022). This later scenario is based on the fact that Hawaii is very close to the volcano's geomagnetic conjugate point. Lin et al. (2022) also reported the presence of conjugate TIDs, lending more support to this explanation.

In contrast, the tsunami ionospheric signature with the largest amplitude in the vicinity of the Galapagos Islands suggests a tsunami with a higher open-ocean wave ( $\sim 6$  cm zero to crest recorded by the 32413 DART buoy), which contradicts the expected wave height decay with increasing distance from the source ( $\sim 2$  cm; model) (Ward, 2002). Unlike the other identified signatures, the detection near the Galapagos took place around noon local time

(Table S2 in SM), which contributes to the larger amplitude of the detected ionospheric imprints.

The lack of significant delay between the arrival of the Lamb wave imprints in the ionosphere and on the surface, as illustrated by Fig. 5b (and Fig. 16 is SM), suggests that the propagation of the Lamb acts like a moving source (similar to a tsunami), forcing IGWs that travel obliquely upward (Lin et al., 2022). The IGW pattern experienced by the imprints' max sTEC amplitude (depicted in Fig. 4e) supports such a hypothesis.

Lastly, we estimate the apparent propagation speed (Fig. 6a and b; top row) of the tsunami-induced TIDs by considering the distance (to the source) and time at the maximum energy of the waveforms from

0.25 before to 1.75 h after the expected tsunami arrival time. This speed is 232 m/s and 112 m/s, for Kermadec and HTHH, respectively. We highlight that the estimated speed in the HTHH case is much slower than the speed of the tsunami just below the detection points (168 m/s in average). This discrepancy arises from the fact that the IGW is triggered about one hour earlier (Occhipinti et al., 2013 Fig. 7). This is confirmed by examining the bathymetric speed map of the tsunami (Fig. 6b; bottom row). As for the Lamb wave ionospheric signature, Fig. 6c shows that the estimated apparent speed ( $303 \pm 19$  m/s) is consistent with the assumed Lamb wave speed (318 m/s) and the reported apparent speed estimated using the common Time-distance (Hodochron) plots method (Lin et al., 2022; Matoza et al., 2022; Themens et al., 2022; Wright et al., 2022; Zhang et al., 2022).

### 5. Conclusions

The ionospheric imprints of the tsunami generated by the Jan. 15, 2022, Hunga Tonga-Hunga Ha'apai volcanic eruption, as it propagates across the Pacific Ocean, are presented and investigated along with that of the Mar. 4, 2021, 8.1 Mw Kermadec Islands earthquake tsunami; the later event serves as a reference given its proximity and standard ionosphere signature. Our results indicate that, like the ionospheric imprints of earthquake-initiated tsunamis, the imprints of the tsunami generated by the HTHH eruption can be identified and isolated in the ionospheric data, even with a single station approach. This result was achieved despite a high level of ionospheric disturbances, especially in the near-field, produced by the volcanic eruption. These disturbances complicate the detection of tsunami-induced ionospheric signatures, calling for more generic and discriminative filtering algorithms in order to meet the high detection confidence required for early warnings. Yet, the comparison with open-ocean sea-level measurements supports our interpretation that the isolated signatures are those of the tsunami.

Our joint analysis of the ionospheric signatures of the Lamb (pressure) and tsunami waves confirms that their wave energy can leak to the upper atmosphere

(Zhang et al., 2022). In addition, we show that they both trigger internal gravity waves that can be distinguished thanks to their different traveling speeds and spectral content. These results suggest that GNSS-TEC measurements can be used to detect and track tsunamis even with the presence of other similar ionospheric disturbances initiated around the same time by the triggering source. Furthermore, they imply that when GNSS-TEC measurements are extracted near an ocean bottom pressure sensor, they can help discriminating a regular tsunami from an air-sea wave in the sensor observations. Moreover, the detection of the HTHH tsunami's ionospheric signatures across the Pacific Ocean demonstrates the potential of a single-receiver approach that could complement existing near-real-time (NRT) ionospheric monitoring systems such as the newly established GUARDIAN system (Martire et al., 2023). The possibility to rely on a single receiver allows us to more effectively cover areas with limited receivers (e.g., a large fraction of the Pacific Ocean) and provide redundancy in the analysis elsewhere. Currently, the approach requires a visual inspection to validate the identified waveforms. We intend to automate this task in future work, along with the interpretation of the tsunami-induced ionospheric signatures in terms of open-ocean tsunami's wave height, which is the quantity of interest to tsunami early warning systems.

### Acknowledgements

This work was supported by French Agence Nationale de la Recherche (ANR) under reference ANR-19-CE04-0003 and Centre national d'études spatiales (CNES) for APR project UVTECGEOX. We thank E. Astafyeva, P. Coisson, B. Maletckii, F. Manta, D. Mikesell & M. Ravanelli for fruitful discussions within an ad-hoc Geoazur-IPGP-NGI working group on the 2022 Hunga volcano eruption. We also thank two anonymous reviewers for their constructive comments on an initial version of the manuscript.

**Author Contributions** EM and LR contributed to the study's conception and design. Material preparation, data collection, and analysis were performed by EM. The first draft of the manuscript was written by EM, and all authors commented on

previous versions of the manuscript. All authors read and approved the final manuscript.

### Funding

This work was supported by French Agence Nationale de la Recherche (ANR) under reference ANR-19-CE04-0003 and Centre national d'études spatiales (CNES) for APR project UVTECGEOX.

### Data Availability

All GNSS data are freely available from the Geoscience Australia data archives (<ftp://ftp.data.gnss.gov.au/daily/>) and the CDDIS data archives ([https://cddis.nasa.gov/Data\\_and\\_Derived\\_Products/GNSS/daily\\_30second\\_data.html](https://cddis.nasa.gov/Data_and_Derived_Products/GNSS/daily_30second_data.html)). The ocean bathymetry data ETOPO1 (1 min global relief model; Amante & Eakins, 2009) and the open-ocean sea-level measurements (DART) are from the NOAA data archives (<https://www.ngdc.noaa.gov/mgg/bathymetry/relief.html>; <https://www.ngdc.noaa.gov/hazard/DARTData.shtml>). The coastal sea-level measurements (tide gauge) are publicly available via the Intergovernmental Oceanographic Commission of UNESCO (<http://www.ioc-sealevelmonitoring.org/>). To generate the tsunami travel times, we take advantage of Geoware TTT SDK software (Wessel, 2009).

### Declarations

**Conflict of interest** The authors have no relevant financial or non-financial interests to disclose.

**Open Access** This article is licensed under a Creative Commons Attribution 4.0 International License, which permits use, sharing, adaptation, distribution and reproduction in any medium or format, as long as you give appropriate credit to the original author(s) and the source, provide a link to the Creative Commons licence, and indicate if changes were made. The images or other third party material in this article are included in the article's Creative Commons licence, unless indicated otherwise in a credit line to the material. If material is not included in the article's Creative Commons licence and your intended use is not permitted by statutory regulation or exceeds the permitted use, you will need to obtain permission directly from the copyright holder. To view a copy of this licence, visit <http://creativecommons.org/licenses/by/4.0/>.

**Publisher's Note** Springer Nature remains neutral with regard to jurisdictional claims in published maps and institutional affiliations.

### REFERENCES

- Ajith, K. K., Sunil, A. S., Sunil, P. S., Thomas, D., Kunnummal, P., & Rose, M. S. (2022). Atmospheric and ionospheric signatures associated with the 15 January 2022 Cataclysmic Hunga-Tonga Volcanic Eruption: A multi-layer observation. *Pure and Applied Geophysics*, 179(12), 4267–4277. <https://doi.org/10.1007/s00024-022-03172-z>
- Amante, C., & Eakins, B.W. (2009). ETOPO1 1 Arc-minute global relief model: Procedures, data sources and analysis. *National Geophysical Data Center, NOAA*. <https://doi.org/10.7289/V5C8276M>
- Amores, A., Monserrat, S., Marcos, M., Argüeso, D., Villalonga, J., Jordà, G., & Gomis, D. (2022). Numerical simulation of atmospheric lamb waves generated by the 2022 Hunga-Tonga volcanic eruption. *Geophysical Research Letters*. <https://doi.org/10.1029/2022GL098240>
- Artru, J., Ducic, V., Kanamori, H., Lognonné, P., & Murakami, M. (2005). Ionospheric detection of gravity waves induced by tsunamis. *Geophysical Journal International*, 160, 840–848. <https://doi.org/10.1111/j.1365-246X.2005.02552.x>
- Astafyeva, E., Maletckii, B., Mikesell, T. D., Munaibari, E., Ravanelli, M., Coisson, P., Manta, F., & Rolland, L. (2022). The 15 January 2022 Hunga Tonga Eruption History as Inferred From Ionospheric Observations. *Geophysical Research Letters*. <https://doi.org/10.1029/2022GL098827>
- Carvajal, M., Sepúlveda, I., Gubler, A., & Garreaud, R. (2022). Worldwide Signature of the 2022 Tonga Volcanic Tsunami. *Geophysical Research Letters*, 49(6), 8–11. <https://doi.org/10.1029/2022gl098153>
- Davies, K., & Hartmann, G. K. (1997). Studying the ionosphere with the Global Positioning System. *Radio Science*, 32(4), 1695–1703. <https://doi.org/10.1029/97RS00451>
- Evans, J. V. (1957). The electron content of the ionosphere. *Journal of Atmospheric and Terrestrial Physics*, 11(3–4), 259–271. [https://doi.org/10.1016/0021-9169\(57\)90071-5](https://doi.org/10.1016/0021-9169(57)90071-5)
- Fagundes, P. R., Cardoso, F. A., Fejer, B. G., Venkatesh, K., Ribeiro, B. A. G., & Pillat, V. G. (2016). Positive and negative GPS-TEC ionospheric storm effects during the extreme space weather event of March 2015 over the Brazilian sector. *Journal of Geophysical Research*, 121(6), 5613–5625. <https://doi.org/10.1002/2015JA022214>
- Galvan, D. A., Komjathy, A., Hickey, M. P., & Mannucci, A. J. (2011). The 2009 Samoa and 2010 Chile tsunamis as observed in the ionosphere using GPS total electron content. *Journal of Geophysical Research*. <https://doi.org/10.1029/2010JA016204>
- Georges, T. M., & Hooke, W. H. (1970). Wave-induced fluctuations in ionospheric electron content: A model indicating some observational biases. *Journal of Geophysical Research*, 75(31), 6295–6308. <https://doi.org/10.1029/JA075i031p06295>
- Grawe, M. A., & Makela, J. J. (2015). The ionospheric responses to the 2011 Tohoku, 2012 Haida Gwaii, and 2010 Chile tsunamis: Effects of tsunami orientation and observation geometry. *Earth*

- and *Space Science*, 2(11), 472–483. <https://doi.org/10.1002/2015EA000132>
- Grawe, M. A., & Makela, J. J. (2017). Observation of tsunami-generated ionospheric signatures over Hawaii caused by the 16 September 2015 Illapel earthquake. *Journal of Geophysical Research: Space Physics*, 122(1), 1128–1136. <https://doi.org/10.1002/2016JA023228>
- Gusman, A. R., Roger, J., Noble, C., Wang, X., Power, W., & Burbidge, D. (2022). The 2022 Hunga Tonga-Hunga Ha'apai Volcano Air-Wave Generated Tsunami. *Pure and Applied Geophysics*, 179(10), 3511–3525. <https://doi.org/10.1007/s00024-022-03154-1>
- Heki, K., Bagiya, M. S., & Takasaka, Y. (2022). Slow fault slip signatures in coseismic ionospheric disturbances. *Geophysical Research Letters*, 49, e2022GL101064. <https://doi.org/10.1029/2022GL101064>
- Hu, G., Li, L., Ren, Z., & Zhang, K. (2023). The characteristics of the 2022 Tonga volcanic tsunami in the Pacific Ocean. *Natural Hazards and Earth System Sciences*, 23, 675–691. <https://doi.org/10.5194/nhess-23-675-2023>
- Inchin, P. A., Heale, C. J., Snively, J. B., & Zettergren, M. D. (2020). The Dynamics of Nonlinear Atmospheric Acoustic-Gravity Waves Generated by Tsunamis Over Realistic Bathymetry. *Journal of Geophysical Research*, 125(12), 1–18. <https://doi.org/10.1029/2020JA028309>
- Kubota, T., Saito, T., & Nishida, K. (2022). Global fast-traveling tsunamis driven by atmospheric Lamb waves on the 2022 Tonga eruption. *Science*. <https://doi.org/10.1126/science.abo4364>
- Kulichkov, S. N., Chunchuzov, I. P., Popov, O. E., Gorchakov, G. I., Mishenin, A. A., Perepelkin, V. G., Bush, G. A., Skorokhod, A. I., Vinogradov, Y. A., Semutnikova, E. G., Šepic, J., Medvedev, I. P., Gushchin, R. A., Kopeikin, V. M., Belikov, I. B., Gubanov, D. P., Karpov, A. V., & Tikhonov, A. V. (2022). Acoustic-Gravity Lamb Waves from the Eruption of the Hunga-Tonga-Hunga-Hapai Volcano. Its Energy Release and Impact on Aerosol Concentrations and Tsunami. *Pure and Applied Geophysics*, 179(5), 1533–1548. <https://doi.org/10.1007/s00024-022-03046-4>
- Latu, K. (2022). Prime Minister defends Deputy's 'no sirens' reply as tsunami death toll rises to four. *Kaniva Tonga Media*. <https://www.kanivatonga.nz/2022/01/prime-minister-defends-deputy-s-no-sirens-reply-as-tsunami-death-toll-rises-to-four/>
- Lin, J., Rajesh, P. K., Lin, C. C. H., Chou, M., Liu, J., Yue, J., Hsiao, T., Tsai, H., Chao, H., & Kung, M. (2022). Rapid conjugate appearance of the giant ionospheric lamb wave signatures in the northern hemisphere after Hunga-Tonga volcano eruptions. *Geophysical Research Letters*. <https://doi.org/10.1029/2022GL098222>
- Liu, J. Y., Tsai, H. F., & Jung, T. K. (1996). Total electron content obtained by using the global positioning system. *Terrestrial, Atmospheric and Oceanic Sciences*, 7(1), 107. [https://doi.org/10.3319/TAO.1996.7.1.107\(A\)](https://doi.org/10.3319/TAO.1996.7.1.107(A))
- Liu, J. Y., Tsai, Y. B., Ma, K. F., Chen, Y. I., Tsai, H. F., Lin, C. H., Kamogawa, M., & Lee, C. P. (2006). Ionospheric GPS total electron content (TEC) disturbances triggered by the 26 December 2004 Indian Ocean tsunami. *Journal of Geophysical Research*, 111(5), 2–5. <https://doi.org/10.1029/2005JA011200>
- Liu, J. Y., Tsai, H. F., Lin, C. H., Kamogawa, M., Chen, Y. I., Lin, C. H., Huang, B. S., Yu, S. B., & Yeh, Y. H. (2010). Coseismic ionospheric disturbances triggered by the Chi-Chi earthquake. *Journal of Geophysical Research*, 115(8), 1–12. <https://doi.org/10.1029/2009JA014943>
- Lynett, P., McCann, M., Zhou, Z., Renteria, W., Borrero, J., Greer, D., Fa'anunu, O., Bosserelle, C., Jaffe, B., Selle, S. La, Ritchie, A., Snyder, A., Nasr, B., Bott, J., Graehl, N., Synolakis, C., Ebrahimi, B., & Cinar, G. E. (2022). Diverse Tsunamigenesis Triggered by the Hunga Tonga-Hunga Ha'apai Eruption. *Nature*. <https://doi.org/10.1038/s41586-022-05170-6>
- Martire, L., Krishnamoorthy, S., Vergados, P., Romans, L. J., Szilágyi, B., Meng, X., Anderson, J. L., Komjáthy, A., & Bar-Sever, Y. E. (2023). The GUARDIAN system-a GNSS upper atmospheric real-time disaster information and alert network. *GPS Solutions*, 27(1), 32. <https://doi.org/10.1007/s10291-022-01365-6>
- Matoza, R. S., Fee, D., Assink, J. D., Iezzi, A. M., Green, D. N., Kim, K., Toney, L., Lecocq, T., Krishnamoorthy, S., Lalande, J.-M., Nishida, K., Gee, K. L., Haney, M. M., Ortiz, H. D., Brisaud, Q., Martire, L., Rolland, L., Vergados, P., Nippres, A., Wilson, D. C. (2022). Atmospheric waves and global seismoacoustic observations of the January 2022 Hunga eruption, Tonga. *Science*. <https://doi.org/10.1126/science.abo7063>
- Mizutori, M., & Guha-Sapir, D. (2018). Economic Losses, Poverty & DISASTERS 1998–2017. *Centre for Research on the Epidemiology of Disasters & United Nations Office for Disaster Risk Reduction*. Retrieved from [https://www.preventionweb.net/files/61119\\_credeconomiclosses.pdf](https://www.preventionweb.net/files/61119_credeconomiclosses.pdf)
- Ochipinti, G., Coisson, P., Makela, J. J., Allgeyer, S., Kherani, A., Hébert, H., & Lognonné, P. (2011). Three-dimensional numerical modeling of tsunami-related internal gravity waves in the Hawaiian atmosphere. *Earth, Planets and Space*, 63(7), 847–851. <https://doi.org/10.5047/eps.2011.06.051>
- Ochipinti, G., Kherani, A. E., & Lognonné, P. (2008). Geomagnetic dependence of ionospheric disturbances induced by tsunamigenic internal gravity waves. *Geophysical Journal International*, 173(3), 753–765. <https://doi.org/10.1111/j.1365-246X.2008.03760.x>
- Ochipinti, G., Rolland, L., Lognonné, P., & Watada, S. (2013). From Sumatra 2004 to Tohoku-Oki 2011: The systematic GPS detection of the ionospheric signature induced by tsunamigenic earthquakes. *Journal of Geophysical Research*, 118(6), 3626–3636. <https://doi.org/10.1002/jgrg.50322>
- Omira, R., Ramalho, R. S., Kim, J., González, P. J., Kadri, U., Miranda, J. M., Carrilho, F., & Baptista, M. A. (2022). Global Tonga tsunami explained by a fast-moving atmospheric source. *Nature*, 609(7928), 734–740. <https://doi.org/10.1038/s41586-022-04926-4>
- Parra, N. (2022). Two deaths and tsunami damage reported in Peru: country did not issue an alert. *Radio Bió-Bío*. <https://www.biobiochile.cl/noticias/internacional/america-latina/2022/01/15/reportan-dos-muertes-y-danos-por-tsunami-en-peru-pais-no-emitio-alerta.shtml>
- Rakoto, V., Lognonné, P., Rolland, L., & Coisson, P. (2018). Tsunami Wave Height Estimation from GPS-Derived Ionospheric Data. *Journal of Geophysical Research*, 123(5), 4329–4348. <https://doi.org/10.1002/2017JA024654>
- Ratcliffe, J. A. (1951). Some regularities in the F 2 region of the ionosphere. *Journal of Geophysical Research*, 56(4), 487–507. <https://doi.org/10.1029/JZ056i004p00487>
- Ravanelli, M., Astafyeva, E., Munaibari, E., Rolland, L., & Mikesell, T. D. (2023). Ocean-ionosphere disturbances due to the 15 January 2022 Hunga-Tonga Hunga-Ha'apai eruption.

- Geophysical Research Letters*. <https://doi.org/10.1029/2022GL101465>
- Rolland, L. M., Occhipinti, G., Lognonné, P., & Loevenbruck, A. (2010). Ionospheric gravity waves detected offshore Hawaii after tsunamis. *Geophysical Research Letters*. <https://doi.org/10.1029/2010GL044479>
- Romano, F., Gusman, A. R., Power, W., Piatanesi, A., Volpe, M., Scala, A., & Lorito, S. (2021). Tsunami Source of the 2021 M W 8.1 Raoul Island Earthquake From DART and Tide-Gauge Data Inversion. *Geophysical Research Letters*, 48(17), 1–11. <https://doi.org/10.1029/2021gl094449>
- Smart, D. (2022). The first hour of the paroxysmal phase of the 2022 Hunga Tonga Hunga Ha'apai volcanic eruption as seen by a geostationary meteorological satellite. *Weather*, 77(3), 81–82. <https://doi.org/10.1002/wea.4173>
- Themens, D. R., Watson, C., Žagar, N., Vasylyevych, S., Elvidge, S., McCaffrey, A., Prikryl, P., Reid, B., Wood, A., & Jayachandran, P. T. (2022). Global Propagation of Ionospheric Disturbances Associated with the 2022 Tonga Volcanic Eruption. *Geophysical Research Letters*, 49(7), 1–11. <https://doi.org/10.1029/2022GL098158>
- Titheridge, J. E. (1972). Determination of ionospheric electron content from the Faraday rotation of geostationary satellite signals. *Planetary and Space Science*, 20(3), 353–369. [https://doi.org/10.1016/0032-0633\(72\)90034-7](https://doi.org/10.1016/0032-0633(72)90034-7)
- Vadas, S. L., Makela, J. J., Nicolls, M. J., & Milliff, R. F. (2015). Excitation of gravity waves by ocean surface wave packets: Upward propagation and reconstruction of the thermospheric gravity wave field. *Journal of Geophysical Research*, 120(11), 9748–9780. <https://doi.org/10.1002/2015JA021430>
- Ward, S. (2002). *Tsunamis, Encyclopedia of Physical Science and Technology* Vol. 17. ed. Meyers, RA, Academic Press, San Diego, 175–191.
- Wessel, P. (2009). Analysis of Observed and Predicted Tsunami Travel Times for the Pacific and Indian Oceans. *Pure and Applied Geophysics*, 166(1–2), 301–324. <https://doi.org/10.1007/s00024-008-0437-2>
- Wright, C. J., Hindley, N. P., Alexander, M. J., Barlow, M., Hoffmann, L., Mitchell, C. N., Prata, F., Bouillon, M., Carstens, J., Clerbaux, C., Osprey, S. M., Powell, N., Randall, C. E., & Yue, J. (2022). Surface-to-space atmospheric waves from Hunga Tonga-Hunga Ha'apai eruption. *Nature*, 609(7928), 741–746. <https://doi.org/10.1038/s41586-022-05012-5>
- Zedek, F., Rolland, L. M., Mikesell, T. D., Sladen, A., Delouis, B., Twardzik, C., & Coisson, P. (2021). Locating surface deformation induced by earthquakes using GPS, GLONASS and Galileo ionospheric sounding from a single station. *Advances in Space Research*, 68(8), 3403–3416. <https://doi.org/10.1016/j.asr.2021.06.011>
- Zhang, S.-R., Vierinen, J., Aa, E., Goncharenko, L. P., Erickson, P. J., Rideout, W., Coster, A. J., & Spicher, A. (2022). 2022 Tonga Volcanic Eruption Induced Global Propagation of Ionospheric Disturbances via Lamb Waves. *Frontiers in Astronomy and Space Sciences*, 9, 871275. <https://doi.org/10.3389/fspas.2022.871275>

(Received January 23, 2023, revised March 28, 2023, accepted March 31, 2023, Published online April 11, 2023)